

Article

Numerical Simulation Analysis of the Bending Performance of T-Beams Strengthened with Ultra-High-Performance Concrete Based on the CDP Model

Yu Long ¹, Zhimei Jiang ^{1,2}, Kongru Zou ^{1,2}, Jiang Du ^{1,2,*} and Jun Yang ^{1,2}

¹ School of Civil Engineering, Chongqing Jiaotong University, Chongqing 400074, China; 632101150919@mails.cqjtu.edu.cn (Y.L.); 622210086060@mails.cqjtu.edu.cn (Z.J.); zoukongru@mails.cqjtu.edu.cn (K.Z.); yangjun@cqjtu.edu.cn (J.Y.)

² State Key Laboratory of Mountain Bridge and Tunnel Engineering, Chongqing Jiaotong University, Chongqing 400074, China

* Correspondence: jiangdu@cqjtu.edu.cn; Tel.: +86-15023182695

Abstract: In bridge reinforcement projects, damaged T-beams are the most common objects for reinforcement, yet the interface bonding and bending performance of UHPC reinforcement on T-beams have hardly been studied. To ensure the reliability and stability of UHPC-strengthened T-beams in practical applications, this study introduced a post-installed rebar bonding technique to efficiently connect T-beams with UHPC layers. Initially, using ABAQUS software [2020 version] for finite element simulation, this study investigated the effects of various post-installed rebar parameters (horizontal spacing, yield strength, diameter, and matrix concrete strength) on the shear performance of the UHPC and RC interface, obtaining the optimal connection parameters. Subsequently, by comparing shear formulas in domestic and international standards, a new UHPC-RC steel bar interface shear strength theoretical formula with 93.6% accuracy was derived. Finally, finite element simulations analyzed the impact of different post-installed reinforcing bar layout forms and longitudinal spacing, as well as UHPC-strengthened location and layer thickness, on the bending performance of damaged T-beams. The results showed a good match between simulation outcomes and experimental results, applicable for further reinforcement analysis of T-beams. When the horizontal spacing of post-installed rebars is 12d, with diameters ranging from 10 mm to 14 mm, their anchoring capability is efficiently utilized. A square form of a post-installed rebar with a longitudinal spacing of 300 mm effectively improves the ultimate bending load capacity of the strengthened beam. The simulation analysis and theoretical results help in the design and application of post-installed steel connections and UHPC-strengthened structures in UHPC-strengthened reinforced concrete T-beam structures.

Keywords: ultra-high-performance concrete; T-beam; interface shear; flexural strengthening; finite element model



Citation: Long, Y.; Jiang, Z.; Zou, K.; Du, J.; Yang, J. Numerical Simulation Analysis of the Bending Performance of T-Beams Strengthened with Ultra-High-Performance Concrete Based on the CDP Model. *Buildings* **2024**, *14*, 1284. <https://doi.org/10.3390/buildings14051284>

Academic Editor: Giuseppina Uva

Received: 29 February 2024

Revised: 18 April 2024

Accepted: 29 April 2024

Published: 1 May 2024



Copyright: © 2024 by the authors. Licensee MDPI, Basel, Switzerland. This article is an open access article distributed under the terms and conditions of the Creative Commons Attribution (CC BY) license (<https://creativecommons.org/licenses/by/4.0/>).

1. Introduction

The scale of highway bridges in China is huge [1], and many old bridges have a large number of structural and utilization problems, such as the corrosion of steel bars, serious aging of concrete, concrete spalling, excessive crack width, insufficient bearing capacity, and high prestressing losses [2–6]. More than 30% of bridges that are currently in use require strengthening and repair, not just in our nation but also in developed nations like the US and Canada [7]. When it comes to renovating both new and old bridges, ultra-high-performance concrete (UHPC) is a novel kind of strengthening material that offers several benefits [8–13]. It is constructed based on the principle of maximum packing density [14] and exhibits excellent compressive, tensile, shear, and durability properties [15–21]. In order to enhance the flexural performance of reinforced concrete (RC) beams or slabs,

UHPC is frequently placed as a thin layer in the tensile zone of the beams or slabs due to its exceptional mechanical qualities and high durability [22]. Numerous academics have looked into the flexural properties of UHPC-strengthened RC beams [23–25], as well as the interfacial shear properties between UHPC and plain concrete [26–28]. The shear properties between UHPC and RC determine the flexural properties of UHPC-strengthened beams.

N.K. Banjara et al. [29] comparatively analyzed the effect of the reinforcement rate of UHPC strips and whether the UHPC ends are strengthened or not on damaged RC beams, and the test showed that utilizing interfacial adhesive gluing of UHPC strips leads to end interfacial bond damage, and the use of U-type CFRP ring wrapping of the UHPC ends effectively prevents the stripping damage of the strengthened beams and improves the ultimate bearing capacity by 30%. Al-Osta et al. [30] examined the flexural behavior of RC beams strengthened with glued or cast-in-place UHPC strips in single-, double-, and triple-sided configurations. They discovered that the flexural behavior of the strengthened beams was not significantly impacted by the different interfacial bonding techniques (two types of epoxy adhesive versus sandblasting technique). P. Mário [31] conducted 16 UHPC (50 mm thick)-strengthened RC beam flexural (shear) tests, which showed that when the interface was treated with air hammer chiseling, the overall working performance between the UHPC reinforcement layer and the RC beams was better, verifying the potential and effectiveness of UHPC for strengthening RC structures. Liu et al. [32] conducted an experimental study of the shear and tensile behavior of UHPC-RC interface samples and used the interface model for finite element simulations of UHPC-strengthened concrete T-beams, which were more accurate using the CF interface model than using the perfect bond (PB) model. In subsequent simulations, it was found that the stiffness and shear capacity of the strengthened T-beams were greatly improved when the thickness of the UHPC layer was increased to 80 mm and the interfacial anchorage spacing was less than 300 mm. Liu et al. [33] created ten concrete T-beams with varying steel bar configurations, UHPC layer thicknesses, and anchors at the repair interfaces in order to study the shear performance of UHPC-strengthened cast-in-place concrete T-beams. They suggested using U-shaped jacket configurations when a significant increase in beam stiffness was needed, and discovered that a 50 mm transverse layer and a 25 mm U-shaped jacket produced more ductile failure modes. Sun et al. [34] investigated the interfacial shear performance of UHPC-strengthened RC structures using post-installed rebar connections. They designed three UHPC-based reinforcement forms: two-sided, U-form, and casing. They carried out 34 push-out tests. In comparison to the two-sided and U-form-strengthened specimens, they discovered that the specimens with casing reinforcement exhibited a notable clamping effect. A significant amount of frictional resistance is still produced by the clamping effect even in cases where the post-installed reinforcing bars' embedment depth is insufficient. Gao et al. [35] investigated the effect of different post-installed reinforcing bar embedment lengths on the interfacial shear strength and found that a length-to-diameter ratio greater than or equal to 2.5 is sufficient to give full play to the anchorage capacity of strengthened UHPC. Zhu Y [36] and others used the method of "unit node localization tracking", i.e., setting the "localization unit" with material properties much lower than those of the model components, to adjust the activation position of the UHPC reinforcement layer so as to make it coincide with the contact of the unloaded RC interface, and used the damage plasticity model of ABAQUS to simulate the intrinsic model.

It has been shown that the performance of UHPC-strengthened beams depends on whether good interfacial shear properties can be ensured between UHPC and plain concrete and that the post-installed rebar bonding technique is a better solution to the UHPC-RC bonding problem. However, few researchers have investigated the structural performance of UHPC-strengthened T-beams with the post-installed rebar bonding technique. Moreover, there have been many studies related to UHPC-strengthened beams, while research on UHPC-strengthened T-beams is still very scarce. In practical engineering, reinforced concrete T-beams are widely used in bridge structures due to their resistance to high bending and shear stresses [37], and UHPC-strengthened T-beams may exhibit higher

delamination possibilities [33], so the problems related to the interfacial adhesion and flexural resistance of UHPC-strengthened T-beams require in-depth study.

In summary, 15 sets of push-out simulation tests were carried out using the control variable method with the horizontal spacing of shear-resistant steel bars, yield strength of shear-resistant steel bars, compressive strength of matrix concrete, and diameter of shear-resistant steel bars as parameters using ABAQUS software [38]. The software then analyzed the impact of each rebar planting parameter on the specimen interface's shear performance in order to shed light on the shear performance of the UHPC-RC reinforcement interface. The push-out simulation tests showed how to design the horizontal spacing of shear-resistant steel bars and the diameter of shear-resistant steel bars in the UHPC layer for the numerical simulation of damaged T-beams that have been strengthened with UHPC using this bonding method. A new theoretical formula for the shear strength of the UHPC-RC interface was derived based on the push-out test simulation results. Then, ABAQUS software was used to conduct finite element analysis of bending tests on T-beam specimens with different layout forms of the post-installed reinforcing bars, longitudinal spacing of the post-installed reinforcing bars, UHPC-strengthened position, and thickness of the reinforcement layer. The best base layer reinforcement configuration and placement were suggested in order to fully utilize the benefits of UHPC material and guarantee the overall longevity and safety of the strengthened structure.

2. Test Overview

2.1. Push-Out Test

To study how different horizontal spacings of shear-resistant steel bars, yield strengths of shear-resistant steel bars, compressive strengths of matrix concrete, and diameters of shear-resistant steel bars affect the shear properties at the interface of UHPC and RC, 15 sets of push-out specimens were designed based on previous research [35]. Table 1 shows the specifics of these specimens. The literature [35] makes reference to each of the materials' mechanical properties for the push-out specimens. Figure 1 displays details of the specimen geometry and steel bars.

Table 1. Detailed parameters of the push-out specimen.

Simulation Experiment Parameters	Specimen Number	Horizontal Spacing of Shear-Resistant Steel Bars	Yield Strength of Shear-Resistant Steel Bars (MPa)	Compressive Strength of Matrix Concrete (MPa)	Diameter of Shear-Resistant Steel Bars (mm)
Horizontal spacing of shear-resistant steel bars	Ga1	4d	400	30	12
	Ga2	8d	400	30	12
	Ga3	12d	400	30	12
	Ga4	16d	400	30	12
Yield strength of shear-resistant steel bars (MPa)	St1	12d	335	30	12
	St2	12d	400	30	12
	St3	12d	500	30	12
Compressive strength of matrix concrete (MPa)	Cs1	12d	400	20	12
	Cs2	12d	400	30	12
	Cs3	12d	400	40	12
Diameter of shear-resistant steel bars (mm)	D1	12d	400	30	8
	D2	12d	400	30	10
	D3	12d	400	30	12
	D4	12d	400	30	14
	D5	12d	400	30	16
Reference group	PRB	12.5d	470.21	37.1	12

Note: ①: The thickness of the UHPC reinforcement layer on both sides is 50 mm. ②: The depth of the steel bar planting on the UHPC side is taken as 2.5d in the references. ③: Except for the number of steel bar plantings in the reference group, which is 4, the number of steel bar plantings in the rest of the specimens is 6.

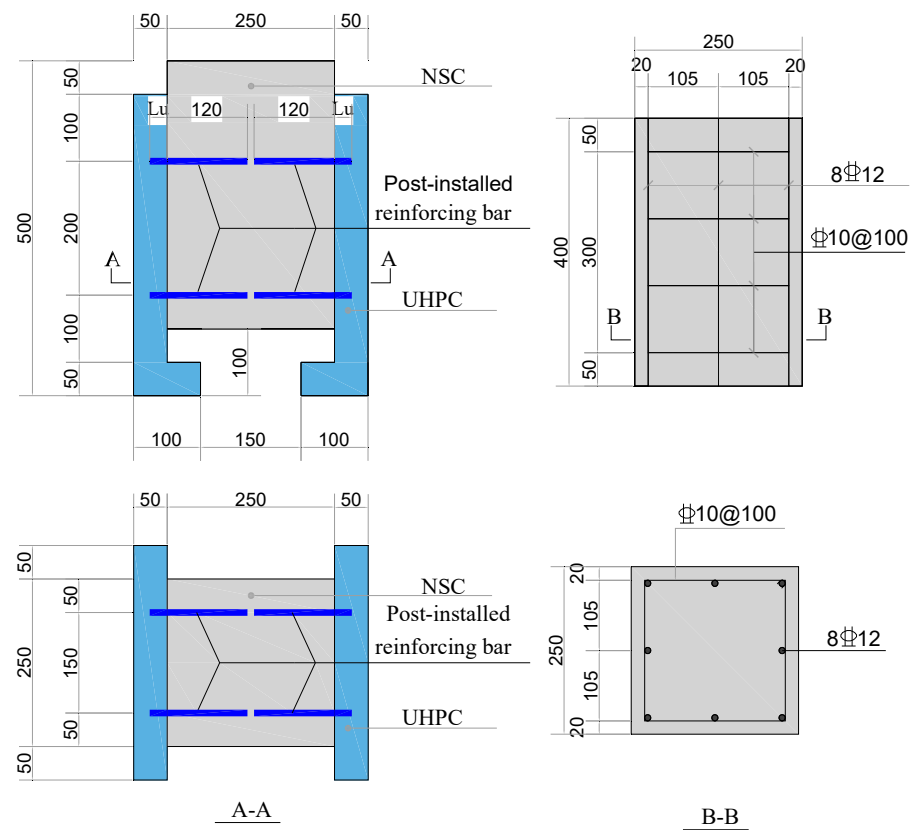


Figure 1. Geometry and steel bar details of the push-out specimen (unit: mm) (reproduced with permission from Ref. [35]. Copyright 2023 Elsevier).

The embedded length of post-installed reinforcing bars in RC matrices is designed according to the GB50367-2013 [39] specification. The calculation method for the minimum embedded length of post-installed reinforcing bars in RC matrices stipulated in GB50367-2013 is as follows:

$$l_{min} = [0.3l_s, 10d, 100\text{mm}] \quad (1)$$

$$l_s = 0.2\alpha_{spt}d f_y / f_{bd} \quad (2)$$

where d is the nominal diameter of the rebar; α_{spt} is the coefficient to consider the effect of concrete splitting damage, which is taken as 1.0 in this paper; f_y is the yield strength of the rebar; and f_{bd} is the shear bond strength, which is taken as 4.5 MPa in this paper.

The minimum embedment lengths of shear-resistant steel bars in specimens D1, D2, D4, and D5 in the RC matrices, calculated according to Equations (1) and (2), were 100 mm, 100 mm, 140 mm, and 160 mm, respectively, and the minimum embedment lengths of shear-resistant steel bars in the rest of the specimens in the RC matrices were 120 mm, which was used in the design of the push-out test specimens.

2.2. Bending Test

This research assessed the flexural performance of damaged T-beams strengthened with UHPC by designing 15 distinct T-beams based on the method by [40]. Table 2 displays the bending specimens' specific parameters. The authors of [40] mention the bending specimens' materials' mechanical properties. Figure 2 displays the geometry of the specimen and the specifics of the reinforcement.

Table 2. Detailed parameters of bending specimens.

Simulation Experiment Parameters	Specimen Number	Layout Form of the Post-Installed Reinforcing Bars	Longitudinal Spacing of the Post-Installed Reinforcing Bars (mm)	UHPC-Strengthened Position	Thickness of Reinforcement Layer (mm)
Layout form of the post-installed reinforcing bars	B1	linear form	300	bottom side	50
	B2	square-shaped form	300	bottom side	50
	B3	triangle form	300	bottom side	50
Longitudinal spacing of the post-installed reinforcing bars (mm)	UGa1	square-shaped form	150	bottom side	50
	UGa2	square-shaped form	300	bottom side	50
	UGa3	square-shaped form	600	bottom side	50
	UGa4	square-shaped form	1200	bottom side	50
UHPC-strengthened position	RP1	square-shaped form	300	bottom side	50
	RP2	square-shaped form	300	both sides	50
	RP3	square-shaped form	300	U-shape (bottom and sides)	50
Thickness of reinforcement layer (mm)	RT1	square-shaped form	original	bottom side	10
	RT2	square-shaped form	300	bottom side	30
	RT3	square-shaped form	300	bottom side	50
	RT4	square-shaped form	300	bottom side	70
	RT5	square-shaped form	300	bottom side	90

Note: ①: There is no post-installed reinforcing bar in the RT1 specimen; the diameter D of post-installed reinforcing bars in RT2, RT3, RT4, and RT5 is 8 mm, 12 mm, 16 mm, and 20 mm, respectively; the diameter D of post-installed reinforcing bars in the rest of the specimens is 12 mm. ②: The depth of the planting rebar in the side of UHPC is taken as $2.5d$ in all the references. ③: The yield strength of post-installed reinforcing bars is 400 MPa. ④: The longitudinal steel bars in the tensile zone of the reinforcement layer are composed of two 10 mm HRB400 bars.

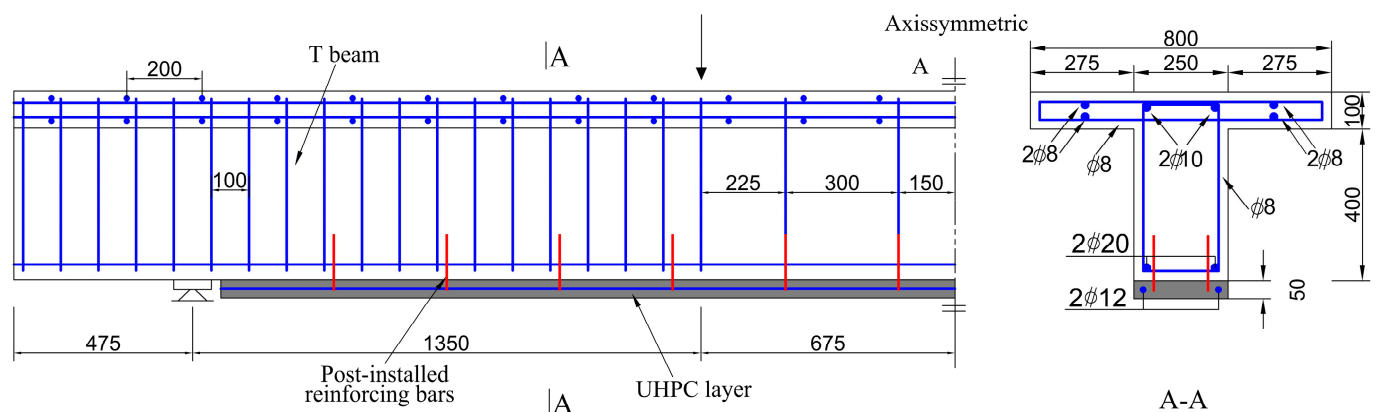


Figure 2. Bending specimen geometry and reinforcement details (unit: mm) (reproduced with permission from Ref. [40]. Copyright 2021 Elsevier).

3. Finite Element Modeling

3.1. Material Constitutive Models

3.1.1. Material Constitution Model of Concrete

The tensile and compressive deformation behavior of concrete is simulated by the Concrete Damage Plasticity (CDP) model in GB50010-2010 [41]. The CDP model considers that the damage modes of concrete are divided into two types, tensile cracking and compressive crushing, and puts the concrete into the plastic state through a reduction in the stiffness related to the plastic strain of the concrete and the tensile and compressive damage factors, which can effectively simulate the stiffness change of concrete structures under loading. Table 3 displays the specific material parameters. The axial compressive strength $f_{c,r}$ of the concrete is 24.9 MPa, and the axial tensile strength $f_{t,r}$ is 2.3 MPa. The

peak compressive strain $\varepsilon_{c,r}$ of the concrete is $1560 \mu\varepsilon$ and the peak tensile strain $\varepsilon_{t,r}$ of the concrete is $102 \mu\varepsilon$.

Table 3. Concrete material parameters.

Material	$\psi/(\circ)$	ε	f_{bo}/f_{co}	k	μ
RC	36	0.1	1.14	0.6667	0.0005

Note: ψ is the expansion angle; ε is the eccentricity; f_{bo} is the biaxial compressive strength of concrete; f_{co} is the uniaxial compressive strength; k is the parameter of the influence of the yielding form of concrete; μ is the viscosity parameter defined in the CDP model.

The axial compression principal relationship for plain concrete is shown in Equations (3)–(6).

$$\sigma = (1 - d_c)E_c\varepsilon \quad (3)$$

$$d_c = \begin{cases} 1 - \frac{\rho_c n}{n-1+x^n} & (x \leq 1) \\ 1 - \frac{\rho_c}{a_c(x-1)^2+x} & (x > 1) \end{cases} \quad (4)$$

$$\rho_c = \frac{f_{c,r}}{E_c\varepsilon_{c,r}} \quad (5)$$

$$n = \frac{E_c\varepsilon_{c,r}}{E_c\varepsilon_{c,r} - f_{c,r}} \quad (6)$$

where $f_{c,r}$ is the axial compressive strength, $x = \frac{\varepsilon}{\varepsilon_{c,r}}$ is the strain ratio, $\varepsilon_{c,r}$ is the peak compressive strain of concrete corresponding to $f_{c,r}$, and a_c is the parameter value of the descending section of the uniaxial compressive stress–strain curve.

The uniaxial tensile principal relationships for plain concrete are shown in Equations (7)–(9).

$$\sigma = (1 - d_t)E_c\varepsilon \quad (7)$$

$$d_t = \begin{cases} 1 - \rho_t [1.2 - 0.2x^5] & (x \leq 1) \\ 1 - \frac{\rho_t}{a_t(x-1)^{1.7}+x} & (x > 1) \end{cases} \quad (8)$$

$$\rho_t = \frac{f_{t,r}}{E_c\varepsilon_{t,r}} \quad (9)$$

where $f_{t,r}$ is the uniaxial tensile strength, x is the strain ratio $x = \frac{\varepsilon}{\varepsilon_{t,r}}$, $\varepsilon_{t,r}$ is the peak tensile strain of the concrete corresponding to $f_{t,r}$, and a_t is the parameter value of the descending section of the uniaxial tensile stress–strain curve.

3.1.2. Material Constitution Model of UHPC

UHPC damage forms include tensile cracking damage and crushing damage. The UHPC constitutive models used in this finite element analysis are the axial tension constitutive model proposed by Zhang [42] and the axial compression constitutive model proposed by Yang [43]. The parameters of UHPC in the CDP model are shown in Table 4. The critical data are adopted from the relevant materiality test data in another paper [35]. The compressive strength f_{cu} of the UHPC compressive stress–strain relationship is defined as 144.1 MPa. The modulus of elasticity E_c and the peak compressive strain ε_{co} are defined as 45 GPa and $3500 \mu\varepsilon$. The elastic tensile strain ε_{ca} of the UHPC tensile stress–strain relationship is defined as $250 \mu\varepsilon$, and the elastic tensile strength f_{ct} and the ultimate tensile strain ε_{pc} are defined as 8.47 MPa and $3050 \mu\varepsilon$, respectively. The UHPC axial tension intrinsic relationship is shown in Equation (10).

$$\sigma = \begin{cases} I & \frac{f_{ct}}{\varepsilon_{ca}} \varepsilon & 0 < \varepsilon \leq \varepsilon_{ca} \\ II & f_{ct} & \varepsilon_{ca} < \varepsilon \leq \varepsilon_{pc} \\ III & \frac{f_{ct}}{(1+w/w_p)^p} & 0 < w \end{cases} \quad (10)$$

where f_{ct} is the UHPC axial tensile strength, ε_{ca} is the linear deviation from the initial crack strain, and w_p is the crack width at fracture.

Table 4. Material parameters of UHPC.

Material	$\psi/(\circ)$	ε	f_{bo}/f_{co}	k	μ
UHPC	36	0.1	1.16	0.6667	0.0005

Note: ψ is the expansion angle; ε is the eccentricity; f_{bo} is the biaxial compressive strength of concrete; f_{co} is the uniaxial compressive strength; k is the parameter of the influence of the yielding form of concrete; μ is the viscosity parameter defined in the CDP model.

The UHPC axial pressure principal relationships are shown in Equations (11)–(13).

$$\sigma = \begin{cases} f_{cu} \frac{n\zeta - \zeta^2}{1 + (n-2)\zeta} & 0 < \varepsilon \leq \varepsilon_{co} \\ f_{cu} \frac{\zeta}{2(\zeta-1)^2 + \zeta} & \varepsilon > \varepsilon_{co} \end{cases} \quad (11)$$

$$\zeta = \frac{\varepsilon}{\varepsilon_{co}} \quad (12)$$

$$n = \frac{E_c}{E_s} \quad (13)$$

where f_{cu} is the UHPC axial compressive strength, ε_{co} is the compressive strain corresponding to the UHPC axial compressive strength, E_c is the initial modulus of elasticity, and E_s is the cut-line modulus of elasticity at the peak point.

3.1.3. Material Constitution Model of Strengthening Steel

The steel reinforcing bar is simulated in the finite element model using a bilinear strengthened intrinsic model. The f_y in the stress–strain relationship for the rebar is defined as the yield strength of the rebar, which is 470.21 MPa, and the f_u is defined as the ultimate strength of the rebar, which is 620.68 MPa.

The stress–strain relationship of the reinforcement is shown in Equation (14).

$$\sigma_s = \begin{cases} E_s \varepsilon_s & 0 \leq \varepsilon_s \leq \varepsilon_y \\ f_y + \frac{f_u - f_y}{\varepsilon_u - \varepsilon_y} (\varepsilon_s - \varepsilon_y) & \varepsilon_y \leq \varepsilon_s \leq \varepsilon_u \end{cases} \quad (14)$$

where σ_s is the reinforcement stress; ε_s is the reinforcement strain; E_s is the reinforcement modulus of elasticity; f_y is the reinforcement yield stress; ε_y is the reinforcement yield strain; f_u is the reinforcement ultimate stress; ε_u is the reinforcement ultimate strain.

3.2. Introduction of Test Cell Types, Interactions, and Boundary Conditions

Figure 3 displays the UHPC-RC interface shear test finite element model. The UHPC, RC, and shear-resistant steel bars are simulated by an 8-node 6-sided solid unit (C3D8R unit), and the strengthening steel mesh inside the matrix concrete is simulated by a T3D2 truss unit. The strengthening steel mesh is embedded in the matrix concrete, and the slip between them is ignored. The cell size of the matrix concrete assembly is 20 mm; the total number of units is 3541. The cell size of the shear-resistant steel bars and hoops is 50 mm. For the thin UHPC assembly, the element size of the UHPC is 20 mm, and the total number of units is 1587.

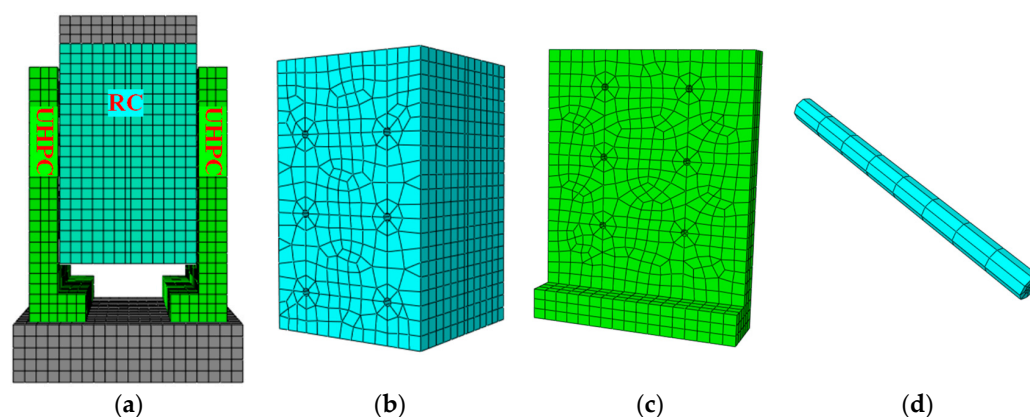


Figure 3. UHPC-RC finite element model and cell meshing. (a) Finite element model; (b) matrix concrete; (c) UHPC reinforcement layer; (d) shear-resistant steel bars.

Between the loading points and the RCs, coupling constraints are used. Between the reinforcing steel mesh and the RCs, built-in region constraints are used. This constraint lets the rebar nodes follow the deformation of the nearby RC nodes. The contact between UHPC and RC, UHPC and shear-resistant steel bars, and RC and shear-resistant steel bars is a nonlinear problem, and the viscous behavior of the contact can be used before the damage cracking of the specimen. The bond surface becomes less stiff after the specimen is damaged and cracked. To simulate the friction between the interfaces, set the “hard contact” function to the normal direction and the “penalty function” function to the tangential direction. The directional friction coefficient at the UHPC-RC interface is taken as 0.15, the directional friction coefficient at the UHPC–shear-resistant steel bar interface is taken as 0.4, and the directional friction coefficient at the RC–shear-resistant steel bar interface is taken as 0.2.

3.3. Bending Test Cell Types, Interactions, and Boundary Conditions

Figure 4 displays the UHPC bottom plate strengthened T-beam finite element model. The solid cell C3D8R, which has difficulty achieving the shear self-locking phenomenon under bending loads, is used in the T-beam and UHPC bottom plate in the test beam model. As a result, the displacement results are more accurate. Even if there is a twisted deformation of the mesh, the accuracy of the analysis will not be affected, but this type of cell requires a finer mesh to overcome the problem of the hourglass and thus obtain an accurate and reliable numerical solution and save the computational cost as much as possible. In addition, the rebar is simulated using the truss cell T3D2. The cell size of the T-beam assembly is 30 mm; the total number of units is 19,786. The cell size of the rebar and hoop bars is 50 mm. For the UHPC bottom plate, the element size of the UHPC is 20 mm, and the total number of units is 4386. In order to more accurately simulate the dynamic damage evolution of T-beams and push-out specimens, parameter analysis was conducted on the mesh size of the model used. It was found that the selected mesh size can already ensure the accuracy of the model, and the convergence of the model is also very good during calculation.

In order to accurately capture the bending behavior of the damaged T-beam strengthened with the UHPC layer, three loading steps are defined in the finite element model: (1) Pre-damage loading and unloading: the UHPC bottom plate is blunted by the function of “Model Change”, and the original beams are preloaded by applying a 30 kN load to the T-beam (in reference [40], the first bending crack appeared in the T-beam when the load reached 30.11 kN, so 30 kN was taken as the preload). After the loading is completed, the load is unloaded to zero. (2) Activation of the UHPC bottom plate: activate the reinforcement layer and the corresponding interaction relationship through the “Model Change” function to realize the T-beam reinforcement process. It is important to note that the corresponding node position changes during the strengthening process because of the residual deformation of the pre-damaged loaded T-beam. If the node unit of the reinforcement

layer is activated directly on the pre-damaged T-beam, the corresponding node connecting the reinforcement layer and the pre-damaged T-beam will be deviated, especially in the analysis of large deformation. In order to make the reinforcement layer activated in situ, in reference [35], the “unit node localization tracking” technique is used to set up a unit set with the same node as the reinforcement layer but different unit numbers, which is activated at the same time with the damaged beams. However, the density and stiffness of the unit set are much smaller than the actual material properties of the model, which ensures that there is almost no effect on the T-beam deformation and force. (3) Loading of strengthened beam: the strengthened T-beam is loaded by displacement until the top concrete is damaged.

In the ABAQUS library, the connector unit CONN3D2 is used to model how the post-installed reinforcing bars act when it comes to shear between the T-beam and the UHPC layer. The position of the connector element corresponds to the actual position of the post-installed reinforcing bars. Notably, the virtual part and the T-beam are connected via the connector element in the finite element model. For the mechanical behavior of the connector elements parallel to the interface, the connector behavior is defined as plastic and the load–displacement relationship is defined based on the average load–slip curve obtained from the push-out test simulation results. For the mechanical behavior of the connector element perpendicular to the interface, the connector behavior is defined as elastic and the stiffness is specified as equal to the axial stiffness of the post-installed reinforcing bars. In addition, the interface behavior of UHPC-RC cannot be neglected in this test, which determines the stress performance of the members. In this paper, the “bond contact behavior” provided by ABAQUS is used in the finite element model to simulate the interfacial properties of UHPC-RC. Hussein et al. [44] obtained the bond model parameters between UHPC and ordinary concrete through experimental research, and its interfacial properties can be divided into rough, medium rough, and smooth according to the degree of roughness of interfacial treatment, with the ultimate slip as the criterion of interfacial damage; in this paper, we adopt the “smooth” bond model to simulate the mechanical behavior of the UHPC-RC interface, with a stiffness coefficient K_{nm} of 1358 N/mm^3 , a K_{ss} , K_{tt} of $20,358 \text{ N/mm}^3$, a damage stress τ_n^0 , τ_s^0 , τ_t^0 of $20,358 \text{ MPa}$, a relative slip of 0.018 mm , and a coefficient of viscosity of 0.001 . The friction coefficients of the contact surfaces between UHPC and RC, UHPC and post-installed reinforcing bars, and RC and post-installed reinforcing bars remain consistent with the push-out simulation tests. In the simulation of the loading process through the rigid pad and the loading position at the beam body-binding (Tie) constraints, the load is applied to the rigid pad; at the same time, the rigid pad is used as a support and the bottom of the beam body-binding connection, and the simple support boundary conditions in the rigid pad are set, as shown in Figure 4. Since the rebar and concrete as well as the UHPC bottom plate were well bonded with almost no slip in the tests, the embedded constraints in ABAQUS “embedded” were used to simplify the treatment between the rebar and concrete as well as the UHPC bottom plate.

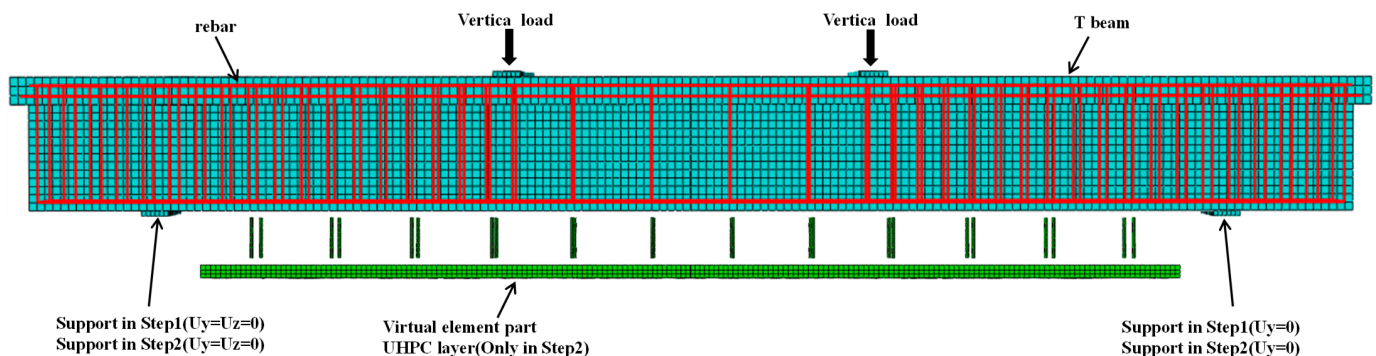


Figure 4. Finite element model of damaged T-beam strengthened with UHPC bottom plate.

4. Finite Element Model Validation

4.1. Validation of the Push-out Test Finite Element Model

This paper is based on the push-out tests in the literature [35] to verify the correctness of the material principal structure, boundary conditions, interactions, and other parameters in the model of this paper.

Figure 5 shows the load–slip comparison curves for the push-out test and the finite element model.

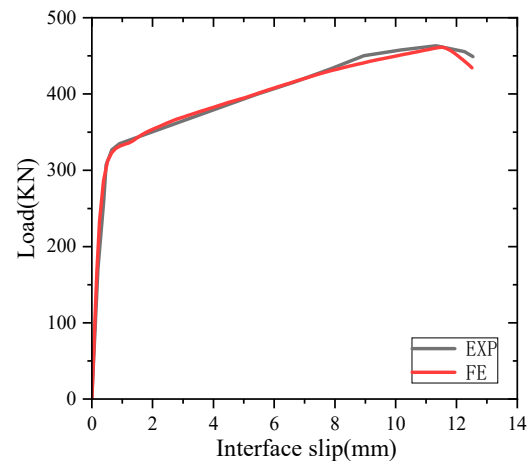


Figure 5. Comparison of load–slip curves for push-out tests and FE.

Figure 5 shows that the load–slip curve obtained from the finite element simulation has a coefficient of variation of 0.351, while the load–slip curve obtained from the push-out test has a coefficient of variation of 0.358, indicating that the two curves are in good agreement; the elasticity stage at the early stage of the numerical simulation and the yield stage of the rebar at the middle and late stages have a very high degree of agreement; the errors between the simulated values of the initial stiffness, the yield load, and the peak load and the test values are all within 5%, which indicates that numerical simulation of the test using the finite element software [2020 version] can accurately reflect the results of the test, and the expansion of parametric analyses can be carried out based on this analysis.

Figure 6 compares the simulation results of the FE model with the results of the push-out test. The FE model also experienced shear failure of the RC matrix, as shown in Figure 6a. Figure 6b shows that the installed reinforcement bar has changed shape fairly significantly. The outcomes demonstrate that, for the most part, the failure modes that the finite element model simulated agree with the test findings. The UHPC-RC rollout test's failure mode and load transfer mechanism can be reliably studied using the finite element model. The UHPC-RC push-out test can be parametrically analyzed with the finite element model.

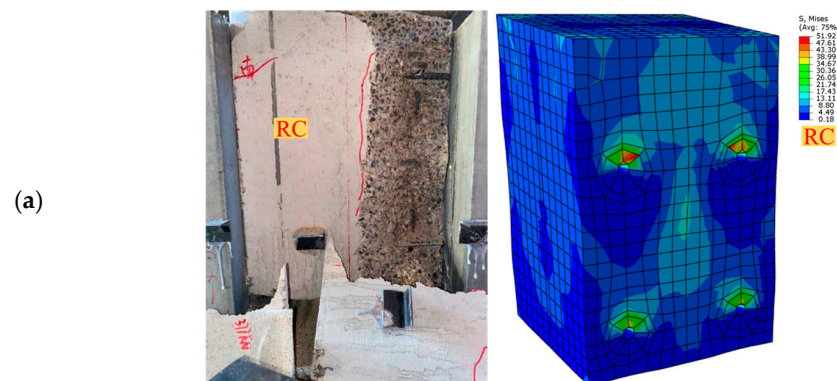


Figure 6. Cont.

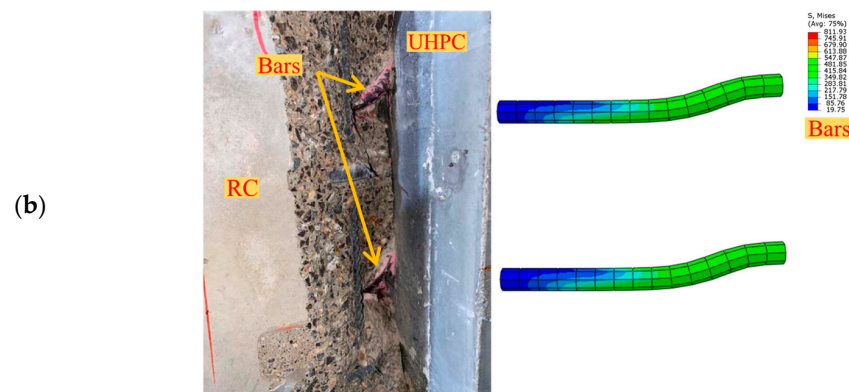


Figure 6. Comparison of failure modes between push-out tests and simulations (unit: MPa) (reproduced with permission from Ref. [35]. Copyright 2023 Elsevier). (a) Comparison of damage situation of RC matrix in the test piece and FE model. (b) Comparison of damage situation of shear-resistant steel bars in the test piece and FE model.

4.2. Validation of Finite Element Models for Bending Tests

This paper is based on the four-point bending test in the literature [40] to verify the correctness of the parameters such as material principal structure, boundary conditions, and interactions in the model of this paper.

The comparison curves for load–midspan displacement between the finite element model and the test beam are displayed in Figure 7.

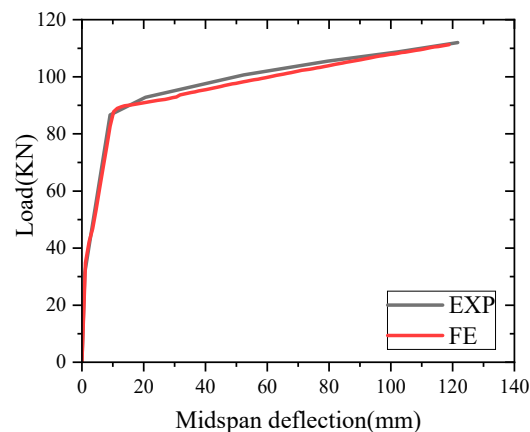


Figure 7. Load–midspan displacement comparison curves for test beams and FE.

As shown in Figure 7, there is good agreement between the coefficient of variation of the load–midspan displacement curve obtained from the finite element simulation, which is 0.508, and the coefficient of variation of the load–midspan displacement curve obtained from the test beam, which is 0.517. The initial elastic stage of numerical simulation has a higher degree of agreement compared to the later elastic–plastic stage, and the initial stiffness, yield load, and peak load errors are all within 5% differences between the test and simulation values. In conclusion, additional research into the mechanical performance parameters of strengthened concrete beams can be conducted using the simulation results from the finite element model of strengthened concrete T-beams established in this paper, as they are sufficiently accurate.

The simulation results of the FE model and the outcomes of the bending tests are contrasted in Figure 8. The original beam specimen had tensile bending damage, as seen in Figure 8. When the load reached 30.11 kN, the first bending crack appeared close to the midspan. Subsequently, more cracks appeared and expanded towards the compression zone, while the crack width increased, leading to a significant reduction

in stiffness. The beam specimen's deflection increased significantly when the tensile reinforcement began to yield at 88.83 kN, but the increase in load-carrying capacity was not significant. The final cracking distribution of the specimen is shown in Figure 8. The finite element model can accurately represent the bending performance of the real concrete T-beam, and the simulation results validate the modeling method's applicability and feasibility. Based on this, the subsequent parametric analysis for the UHPC-strengthened beams can be completed.

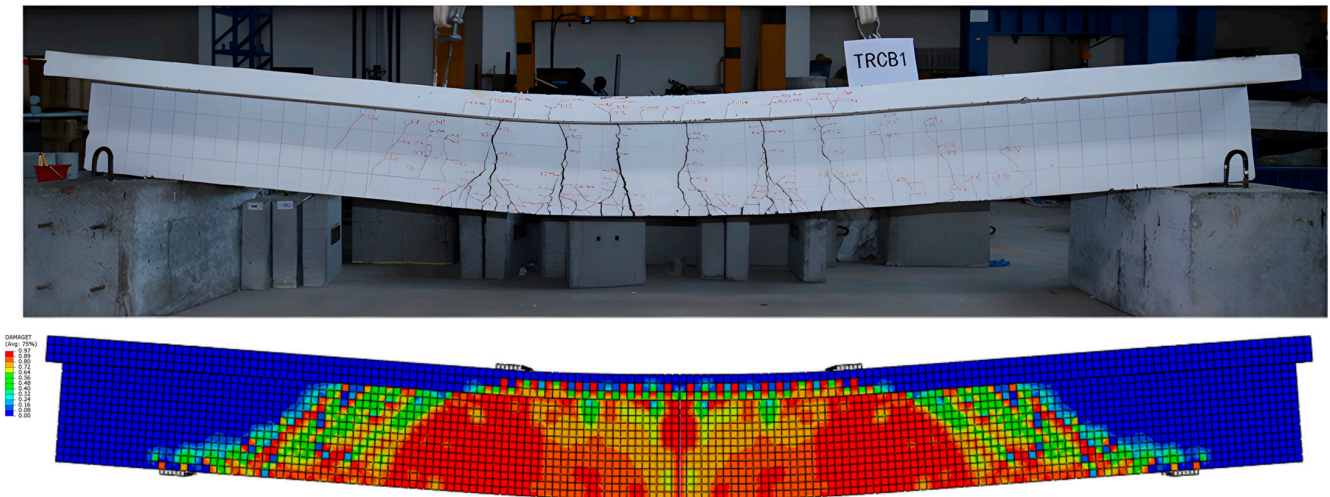


Figure 8. Comparison of failure modes between bending tests and simulations (unit: MPa) (reproduced with permission from Ref. [40]. Copyright 2021 Elsevier).

5. Parametric Analysis

5.1. Push-out Test Parameter Analysis

5.1.1. Horizontal Spacing of Shear-Resistant Steel Bars

With other conditions remaining unchanged, the horizontal spacing of shear-resistant steel bars was selected as 4d, 8d, 12d, and 16d. The impact of horizontal spacing of shear-resistant steel bars on the interfacial shear strength and the load–slip curve of the push-out simulated specimens are displayed in Figure 9. Figure 9a shows that as the horizontal spacing of shear-resistant steel bars goes from 4d to 12d, the ultimate load capacity of the push-out simulated specimen slowly rises along the rising stage of the curve. However, as the horizontal spacing of shear-resistant steel bars goes from 12d to 16d, the ultimate load capacity of the push-out simulated specimen drops quickly to a lower level than when the horizontal spacing of shear-resistant steel bars is 4d.

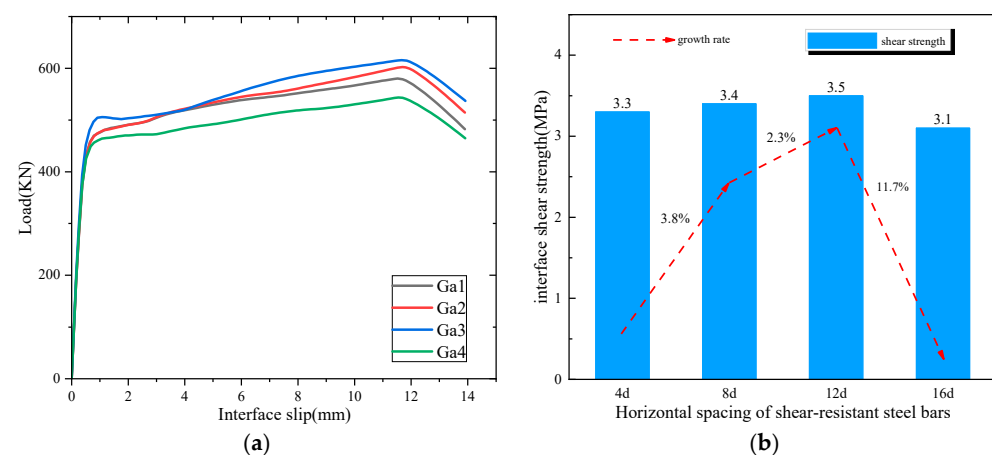


Figure 9. Results of horizontal spacing analysis of shear-resistant steel bars: (a) load–slip curves; (b) comparison of interface shear strengths.

Figure 9b shows the effect of horizontal spacing of shear-resistant steel bars on interfacial shear strength. The interfacial shear strength increased with the increase in horizontal spacing of shear-resistant steel bars from 4d to 12d and showed a relatively large decrease when the horizontal spacing of shear-resistant steel bars was increased to 16d. The interfacial shear strength increased by 3.8% and 2.3% when the horizontal spacing of shear-resistant steel bars increased from 4d to 12d, respectively, and decreased by 11.7% when the horizontal spacing of shear-resistant steel bars increased from 12d to 16d.

In Figure 10, the damage stress clouds of UHPC-RC specimens are shown when they are under a maximum load and have different horizontal spacing of shear-resistant steel bars. From Figure 10, it can be seen that for the Ga1 group, the inner concrete was gradually crushed under the load, and a small number of cracks appeared in the concrete on both sides, and too-small horizontal spacing of shear-resistant steel bars can easily cause local damage to the matrix concrete, resulting in a reduction in the specimen's load-carrying capacity; the damage patterns of the Ga2–Ga3 groups were all interfacial slippage and concrete splitting, and the cracks appeared on the lower side of the concrete from the bottom to the top in the course of the loading process, and the bonding surfaces of the left and right sides of the specimen cracked after the damage, but they did not completely detach, with good bonding performance; the Ga4 group had bond damage in the steel bars at the early loading stage, and the left and right sides of the bond surface cracked when loading to the ultimate load, and relative slip occurred. The large horizontal spacing of shear-resistant steel bars cuts down the bond effect of steel bars, makes the UHPC layer and the concrete disengage, and leads to the failure of the shear-resistant steel bars.

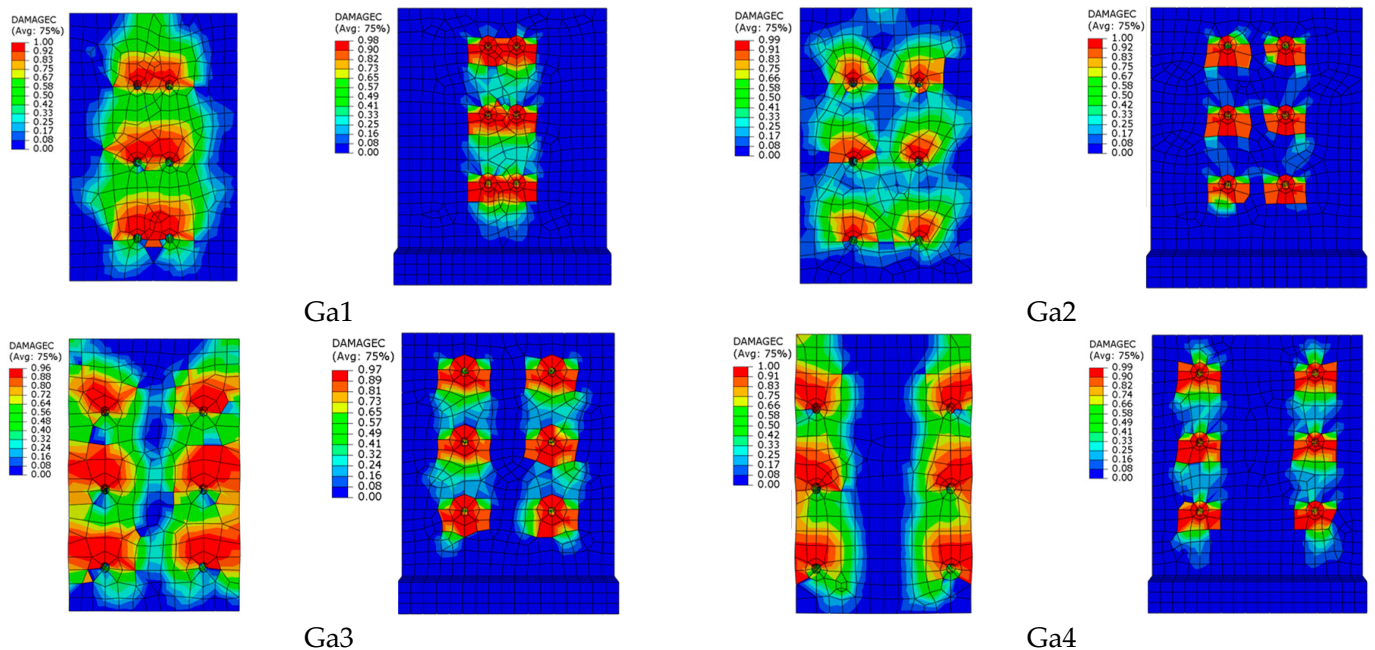


Figure 10. Damage stress cloud for specimens with different horizontal spacings of shear-resistant steel bars (unit: MPa).

It can be seen that the horizontal spacing of shear-resistant steel bars is too small or too large, which reduces the interfacial shear strength and ductility of UHPC-RC, and it is suggested that the horizontal spacing of shear-resistant steel bars should be taken as 8d–12d, which is more reasonable.

5.1.2. Yield Strength of Shear-Resistant Steel Bars

The yield strength of shear-resistant steel bars was chosen to be 335 MPa, 400 MPa, and 500 MPa, with no modifications made to the other parameters. The impact of the yield strength of shear-resistant steel bars on the load–slip curves and the interfacial shear

strengths of the push-out simulated specimens are displayed in Figure 11. The increasing stage of the curve in Figure 11a indicates that the push-out simulated specimen can support an increasing amount of weight as the yield strength of shear-resistant steel bars increases from 335 MPa to 500 MPa.

The impact of the yield strength of shear-resistant steel bars on interfacial shear strength is depicted in Figure 11b. As the yield strength of shear-resistant steel bars increased, so did the interfacial shear strength. When the yield strength of shear-resistant steel bars increased from 335 MPa to 500 MPa, the interfacial shear strength increased by 2.9% and 3.9%, respectively.

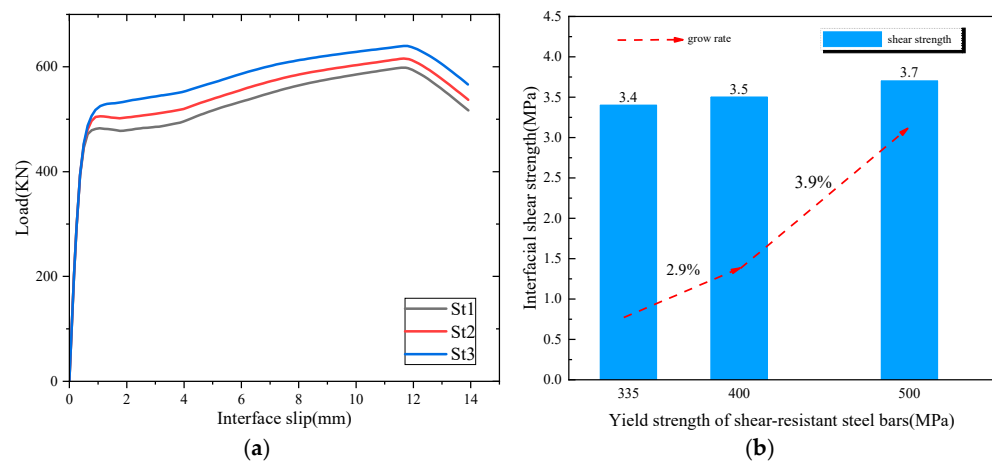


Figure 11. Results of yield strength analysis of shear-resistant steel bars: (a) load–slip curve; (b) comparison of interface shear strengths.

When the interface is subjected to shear, the rebar pinning force is the primary source of the interface shear-bearing capacity, and increasing the yield strength of shear-resistant steel bars can improve the rebar pinning force, according to the analysis of the UHPC-RC reinforcement interface shear mechanism. On the other hand, there will inevitably be some relative slip between the concrete and the rebar when the interface shears. Shear friction between the rebar and the concrete may increase as the yield strength of shear-resistant steel bars increases. Together, they increase the weight of the effect of the yield strength of shear-resistant steel bars on the interface shear strength.

5.1.3. Compressive Strength of Matrix Concrete

Other parameters were left unaltered, and the matrix concrete strengths of 20 MPa, 30 MPa, and 40 MPa were chosen. The impact of matrix concrete strength on the interfacial shear strengths and the load–slip curves of the push-out simulated specimens are depicted in Figure 12. It is evident from Figure 12a that when the matrix concrete strength increases from 20 MPa to 40 MPa, the push-out simulated specimen’s ultimate load capacity progressively increases in the rising stage of the curve.

The impact of matrix concrete strength on interfacial shear strength is depicted in Figure 12b. As matrix concrete strength rises, so does the interfacial shear strength. When the matrix concrete strength increased from 20 MPa to 40 MPa, the interfacial shear strength increased by 4.5% and 2.8%, respectively.

The analysis of the UHPC-RC reinforcement interface shear mechanism shows that, on the one hand, due to the increase in strength of matrix concrete, it can be more resistant to the extrusion stress generated by the steel bar on the hole wall, so the steel bar is sufficiently anchored, which is conducive to the role of the pinning shear provided by the steel bar; on the other hand, when the interface is subjected to shear, the rebar inevitably experiences relative slip between the matrix concrete. The matrix concrete strength can be increased to increase the shear friction of the rebar, and the two together increase the weight of the influence of the matrix concrete strength on the interface shear strength.

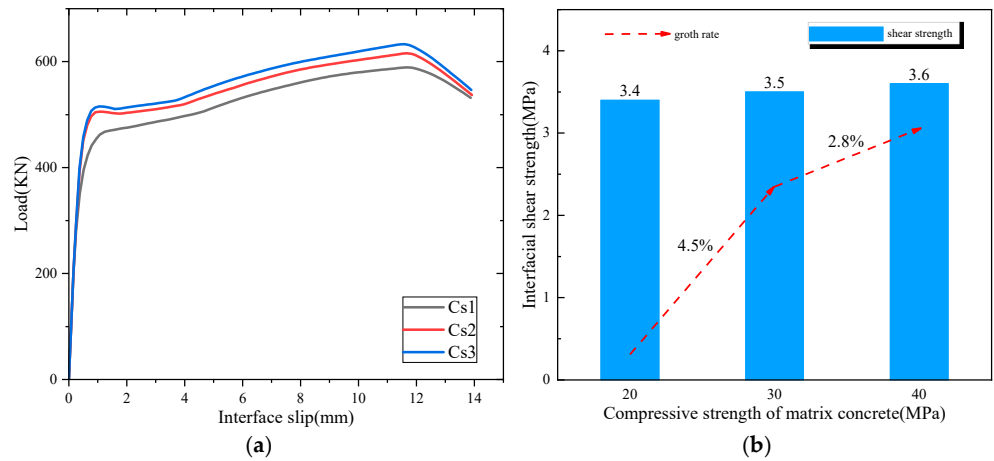


Figure 12. Results of compressive strength analysis of matrix concrete: (a) load–slip curve; (b) comparison of interfacial shear strengths.

5.1.4. Diameter of Shear-Resistant Steel Bars

Other parameters stayed the same, and the diameters of the shear-resistant steel bars were chosen to be 8 mm, 10 mm, 12 mm, 14 mm, and 16 mm. The impact of the diameter of shear-resistant steel bars on the interfacial shear strength and the load–slip curves of the push-out simulated specimens are displayed in Figure 13. It is evident from Figure 13a that when the diameter of shear-resistant steel bars increases from 8 mm to 16 mm, the push-out simulated specimens’ ultimate load capacity progressively rises in the rising stage of the curve.

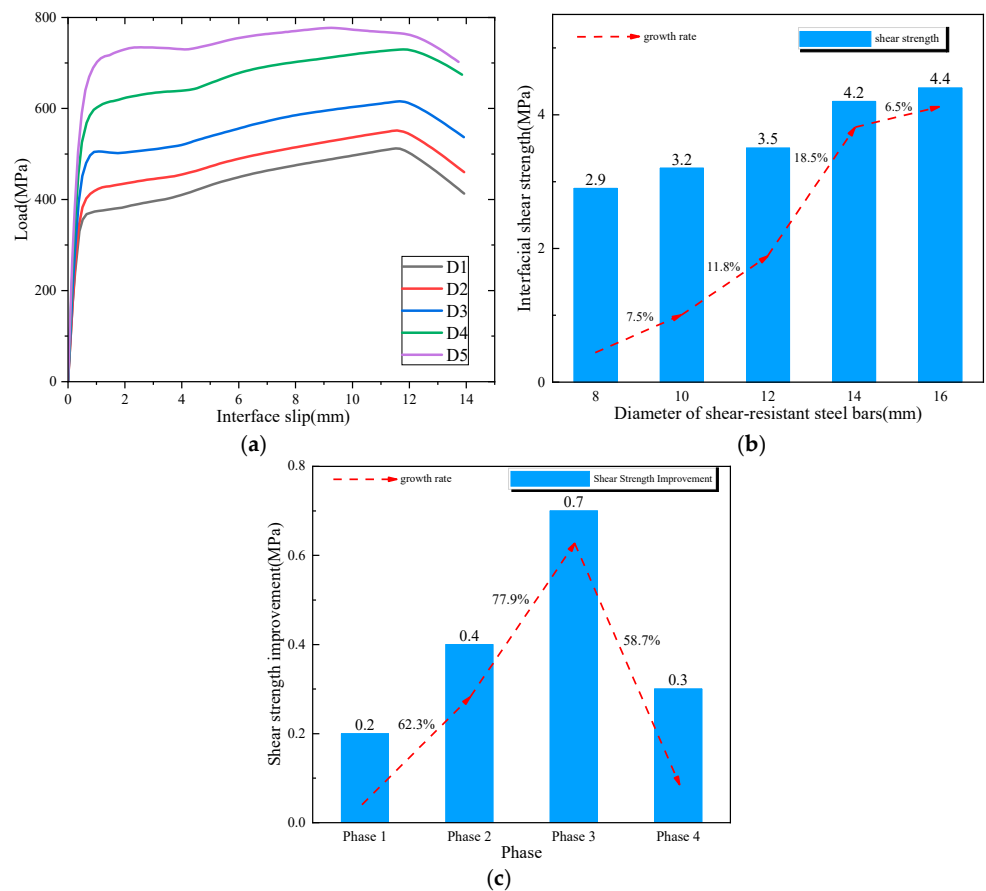


Figure 13. Results of diameter analysis of shear-resistant steel bars: (a) load–slip curves; (b) comparison of interface shear strengths; (c) comparison of interface shear strength uplift values.

The impact of the diameter of shear-resistant steel bars on interfacial shear strength is depicted in Figure 13b. As the diameter of shear-resistant steel bars increases, so does the interfacial shear strength. When the diameter of shear-resistant steel bars increased from 8 mm to 16 mm, the interfacial shear strength increased by 7.5%, 11.8%, 18.5%, and 6.5%.

The interfacial shear strength change values for the diameter of shear-resistant steel bars vary in four consecutive stages, each with four increments, as shown in Figure 13c. Stages 1–3 witness a gradual increase in the value of interfacial shear strength change; however, stage 4 witnesses a decrease in this value. The interfacial shear strength change value increases by 62.3% and 77.9% when it moves from stage 1 to stage 3. Ultimately, there is a 58.7% decrease from stage 3 to stage 4.

Figure 14 shows the concrete damage stress cloud of UHPC-RC specimens under ultimate load for different diameters of shear-resistant steel bars. From Figure 14, it can be seen that for groups D1–D2, the diameter is smaller, between 8 mm and 10 mm of the implanted rebar interface. The concrete can handle the steel bars of compressive stress, and the steel bars can be fully anchored. The shear-resistant steel bars of the pinning force determine the interface shear-bearing capacity. At this point, the shear-resistant steel bars' longitudinal strain suddenly rises, and the interface's ultimate shear force is reached. However, the UHPC-RC interface cannot be separated because of the mechanical friction between the shear-resistant steel bars and the concrete. For groups D4–D5, the diameter is higher, 14 mm and 16 mm for the planted steel bar interface. The concrete near the shear-resistant steel bars was damaged because the concrete could not withstand the extrusion of the shear-resistant steel bars. After the disappearance of concrete cohesion, the rebar withstood part of the shear load and then transformed into a bending and tension composite stress state. At this time, the pinning effect of the rebar and its own shear friction coupling effect is obvious, and in the late stage of loading, the strain slowly increases until the interface reaches the shear-bearing capacity. The D5 specimen interface reaches the ultimate shear when the rebar strain retracts indicating that, at this time, the rebar has completely lost the bond with the concrete and the rebar from the concrete has pulled out.

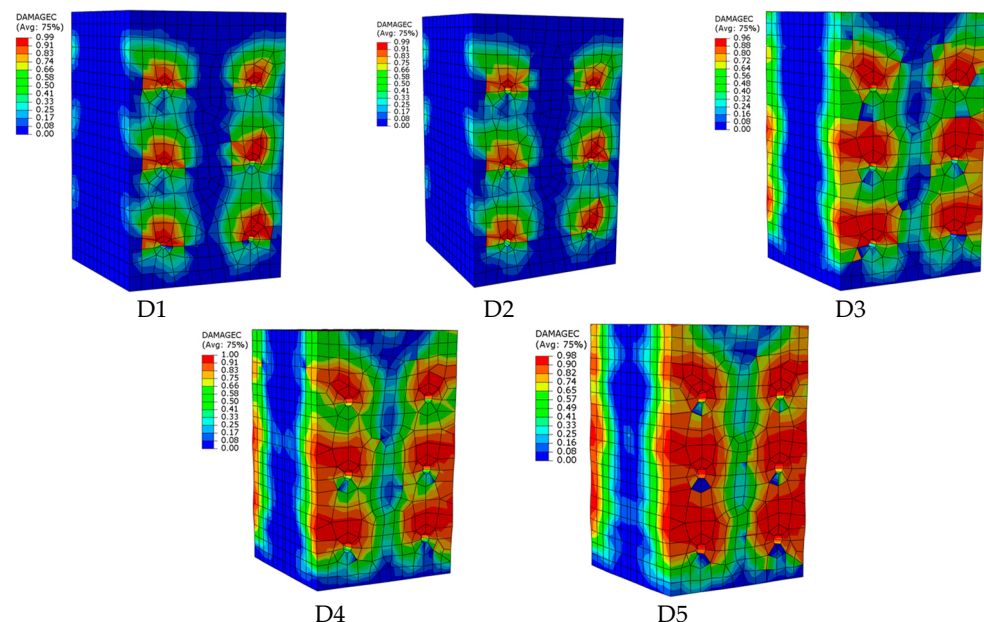


Figure 14. Damage stress cloud of RC for specimens with different diameters of shear-resistant steel bars (unit: MPa).

It can be seen that the diameter of the shear-resistant steel bars is too small or that the diameter of the shear-resistant steel bars is too large, which will reduce the interfacial shear strength and ductility of UHPC-RC. It is recommended that the diameter of the shear-resistant steel bars be 12 mm to be more reasonable.

5.2. Comparison and Modification of Shear Formulas

5.2.1. Normative Comparison

The shear formulas from the American Concrete Code [45], the American Road and Bridge Code [46], the European Concrete Code [47], the Design Code for Strengthening of Highway Bridges [48], the Structural Design Code for Concrete [41], and the Technical Specification for Assembled Concrete Structures [49] are chosen for this section. A comparison of the standard strengths of the six formulas with the simulated values is shown in Table 5.

Table 5. Shear formulas for different codes.

ACI 318-14 [45]	$V = \mu A_{vf} f_y$
AASHTO	$V = c A_{cv} + \mu (A_{sv} f_y + P_c)$
FIB	$\tau_u = \tau_a + \mu (\rho k_1 f_y + \sigma_n) + k_2 \rho \sqrt{f_y f_{cc}}$
JTG/T J22-2008 [48]	$\gamma_0 V_d \leq 0.12 f_{cd} b h_0 + 0.85 f_{sv} \frac{A_{sv}}{S_v} h_0$
GB50010-2010 [41]	$V \leq \frac{1}{\gamma_{RE}} (0.6 f_y A_s + 0.8 N)$
JGJ1-2014 [49]	$V_u = 0.07 f_c A_{cl} + 0.10 f_c A_k + 1.65 A_{sd} \sqrt{f_c f_y}$

Note: ACI 318-14: μ is the coefficient of friction between interfaces: 0.6 when the interface is smooth or untreated, 1.0 when the interface roughness is less than 6.4 mm, and 1.4 when the interface roughness is greater than 6.4 mm. A_{vf} is the total area of the interface shear reinforcement section, in mm².

AASHTO: A_{sv} and A_{cv} are the interface shear reinforcement cross-section total area and the bond surface area in mm². P_c is the interface due to external forces caused by positive pressure in Mpa. c is the interfacial cohesion in Mpa; when the interface is smooth or the treatment is not performed, take 0.52 Mpa; when the interfacial roughness is less than 6.4 mm, take 1.65 MPa; when the interfacial roughness is more than 6.4 mm, take 1.93 MPa. μ is the coefficient of friction between the interfaces; when the interface is smooth or has no treatment, take 0.6; when the interface roughness is less than 6.4 mm, take 1.0; and when the interface roughness is more than 6.4 mm, take 1.4.

FIB: τ_a is the cohesive force at the interface between the old and new concrete, in MPa. μ is the interfacial friction coefficient, taken from Table 6. ρ is the interfacial reinforcement rate. σ_n is the normal stress due to shear at the interface, in MPa. k_1 is the coefficient of bending action, taken as in Table 6. k_2 is the interaction coefficient between steel bars and concrete under the action of pinning bolts, taken from Table 6. f_{cc} is the compressive strength of the concrete cylinder in MPa.

Table 6. Values of specification parameters.

Surface Roughness	R_t	β_c	k_1	k_2	μ	
					$f_{ck} \geq 20$	$f_{ck} \geq 35$
Very rough	≥ 3 mm	0.5	0.5	0.9	0.8	1.0
Rough	≥ 1.5 mm	0.5	0.5	0.9		0.7
Smooth	≤ 1.5 mm	0.4	0.5	1.1		0.6
Very smooth	Not measurable	0.3	0	1.5		0.5

JTG/T J22-2008: γ_0 is the structural importance coefficient, a dimensionless unit; the structural safety levels for the first, second, and third experiments take corresponding values of 1.1, 1.0, and 0.9. f_{cd} is the design value of the compressive strength of concrete, taken as the lower concrete strength value in MPa. S_v is the spacing of the old and new concrete bonding surfaces of the steel bars in mm.

GB50010-2010: A_s is the cross-sectional area of steel bars at the horizontal construction joint of the shear wall in mm². γ_{RE} is the seismic adjustment coefficient of bearing capacity, a dimensionless unit; for the interface of pre-buried anchor steel bars, take 1.0.

JGJ1-2014: A_{cl} is the cross-sectional area of the post-poured concrete composite layer in mm^2 ; A_{sd} is the area of all steel bars passing vertically through the bond surface in mm^2 .

A comparison of the standard strengths of the six formulas with the simulated values is shown in Table 7 and Figure 15. The errors between the remaining five formulas and the simulated values, excluding the Technical Specification for Assembled Concrete Structures, reach more than 30% and are all conservative. The formula in the Technical Specification for Assembled Concrete Structures, which is more comprehensive, embodies the initial cohesion between the concrete as well as the pinning action of the steel bars in the formula, and although this formula is proposed based on the case of assembled structures, it still has predictive capability for the case of post-cast concrete to be used in evaluating the shear capacity of the interface between the UHPC and RC steel bar planting.

Table 7. Comparison of standard strength (kN) of formulas.

Serial Number	FE	ACI 318-14	AASHTO	FIB	JTG/T J22-2008	GB50010-2010	JGJ1-2014
Ga2	602	380	168	169	165	380	565
Ga3	616	380	168	169	125	380	565
St1	598	318	168	142	112	318	555
St2	616	380	168	169	125	380	565
St3	640	475	168	210	145	475	580
Cs1	589	380	168	169	110	380	395
Cs2	616	380	168	169	125	380	565
Cs3	633	380	168	169	140	380	732
D2	552	264	168	119	112	264	529
D3	616	380	168	169	125	380	565
D4	730	517	167	228	138	517	608
average error	-	37.6%	72.5%	72.3%	77.5%	37.6%	11.4%

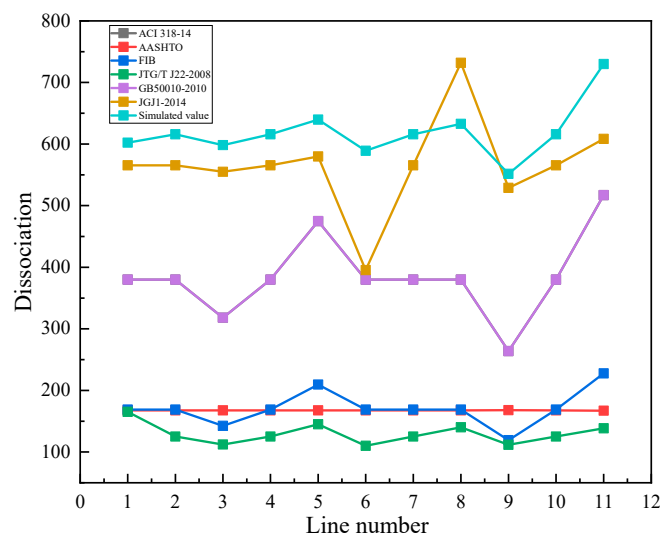


Figure 15. Comparison of formulas.

5.2.2. Modification of the Shear Formula

The prediction formula for the UHPC-RC shear strength at the implanted steel bar interface is suggested, accounting for the effects of steel diameter and concrete strength, based on the prior analysis and formula comparison:

$$V = cA_{cv}f_c + \mu A_{sv}f_y + \xi A_{sv}f_y \quad (15)$$

c is the interface chiseling influence coefficient, a dimensionless unit taken as 0.07.

μ is the coefficient of friction between reinforcement and concrete, a dimensionless unit taken as 0.9.

ζ is the coupling coefficient between the shear friction and pinning force of steel bars when the interface is subjected to shear, a dimensionless unit taken as $\frac{1}{\sqrt{3}}$.

f_c is the concrete strength in MPa; when the strength of new and old concrete is different, take the smaller value of the two.

A_{cv} and A_{sv} are the concrete interface bond surface area and the interface shear steel bar cross-sectional area, units: mm^2 .

Figure 16 shows the comparison between the modified formula and the test results of this paper. Through comparison, it is found that the average error between the formula results and the test results is reduced to 6.8% by taking the steel bars' shear rubbing force as an influencing factor into consideration, and the accuracy reaches 93.6%. It is more applicable for predicting shear strength at the implanted steel bar interface between UHPC and RC.

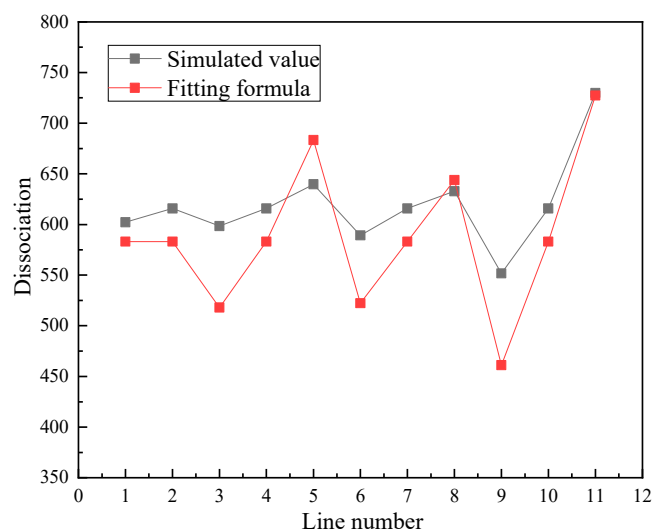


Figure 16. Comparison of correction formulas.

5.3. Bending Test Parameter Analysis

5.3.1. Layout Form of the Post-Installed Reinforcing Bars

This section examines how the layout form of the post-installed reinforcing bars affects the performance of secondary stressed T-beams strengthened by UHPC. The selected underlying reinforcement placement forms are linear, square, and triangular, as shown in Figure 17. Figure 18 shows the effect of the layout form of the post-installed reinforcing bars on the load–deflection curve and peak load. From Figure 18a, it can be seen that the initial stiffness and peak load of the specimen remain constant, and the ductility gradually increases with the change in the layout form of the post-installed reinforcing bars.

Figure 18b shows the effect of the layout form of the post-installed reinforcing bars on the peak load. The variation pattern of peak load is not significant with the change in the layout form of the post-installed reinforcing bars. Compared with the UHPC-strengthened secondary loaded T-beam specimens with a linear layout form of the post-installed reinforcing bars, the peak load slightly increased (within 2%) when the layout form was square and slightly decreased (within 2%) when the layout form was changed to triangular. This means that the UHPC-strengthened secondary stressed T-beams' ability to hold weight does not decrease when the layout form of the post-installed reinforcing bars changes.

It can be seen that the change in the layout form of the post-installed reinforcing bars does not reduce the bearing capacity of the UHPC-strengthened secondary stressed T-beam, but the square form has the highest ductility and higher bearing capacity, so it is recommended that the layout form of the post-installed reinforcing bars be chosen as the square form, which is more reasonable.

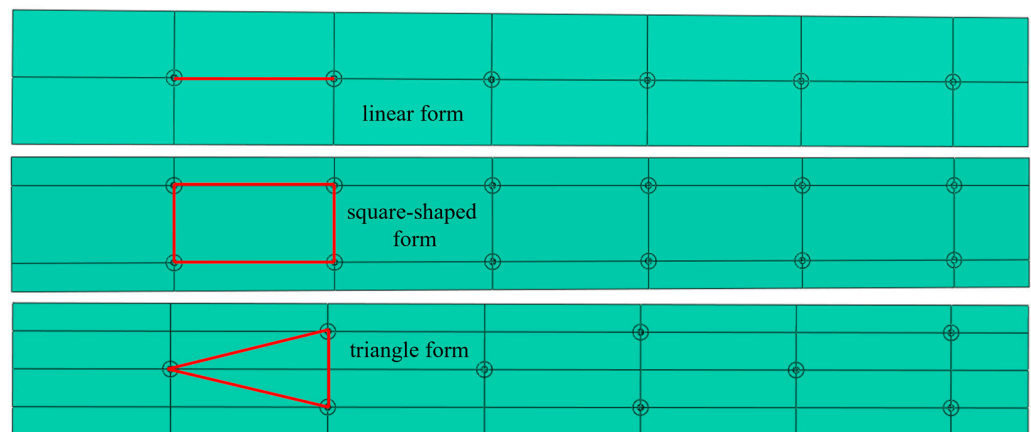


Figure 17. Different layout forms of the post-installed reinforcing bars.

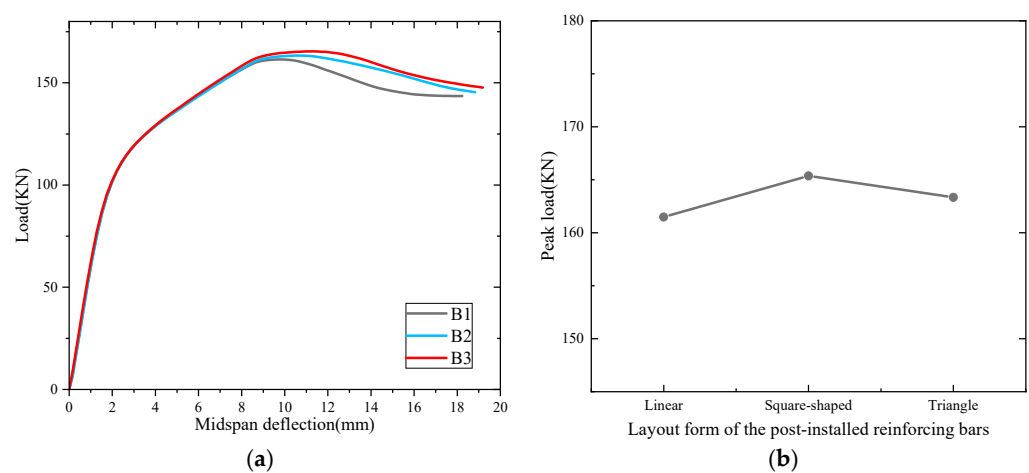


Figure 18. Results of the analysis of the layout form of the post-installed reinforcing bars: (a) load–deflection curve; (b) peak load comparison.

5.3.2. Longitudinal Spacing of the Post-Installed Reinforcing Bars

In this section, the longitudinal spacing of the post-installed reinforcing bars is selected as 150 mm, 300 mm, 600 mm, and 1200 mm, while other conditions remain constant. Figure 19 shows the effect of longitudinal spacing of the post-installed reinforcing bars on the load–deflection curves and peak load of UHPC-strengthened secondary stressed T-beam specimens. In Figure 19a, we can see that as the longitudinal spacing of the post-installed reinforcing bars grows from 150 mm to 1200 mm, and the ultimate load capacity of the UHPC-strengthened secondary stressed T-beam samples gradually decreases in the rising stage of the curve. The part of the load–deflection curves that goes down shows that the UHPC-strengthened secondary stressed T-beam samples will break quickly when the maximum load is reached. The curves of UGa1 and UGa2 tend to be parallel after the load reaches the ultimate load capacity, which indicates that the plastic deformation of these two samples is more pronounced. The curves of UGa3 and UGa4 decline faster after approaching the peak, which indicates that these two samples are more easily damaged.

Figure 19b shows the effect of longitudinal spacing of the post-installed reinforcing bars on the peak load. As the longitudinal spacing of the post-installed reinforcing bars increases, the pattern of change in peak load becomes more significant. Compared to the secondary stressed UHPC-strengthened T-beam specimen with a longitudinal spacing of the post-installed reinforcing bars of 150 mm, the peak load went down by about 1% when the longitudinal spacing of the post-installed reinforcing bars was increased to 300 mm, and it went down by 3.84% when the longitudinal spacing of the post-installed reinforcing bars was increased to 600 mm. There is not much of a difference in peak load between the

UHPC-strengthened secondary stressed T-beam specimens with a longitudinal spacing of the post-installed reinforcing bars of 600 mm and those with a longitudinal spacing of the post-installed reinforcing bars of 1200 mm.

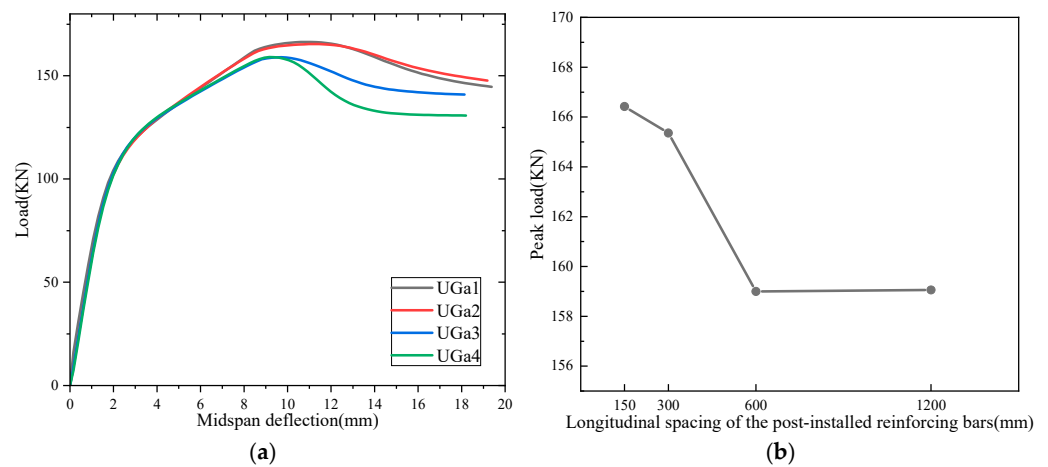


Figure 19. Results of the longitudinal spacing analysis of the post-installed reinforcing bars: (a) load–deflection curve; (b) peak load comparison.

It can be seen that the increase in the longitudinal spacing of the post-installed reinforcing bars will reduce the bearing capacity of the strengthened beam. When the strengthened T-beam has higher ductility and bearing capacity, it is recommended that the longitudinal spacing of the post-installed reinforcing bars of 300 mm be more reasonable.

5.3.3. UHPC Reinforcement Location

In this section, the UHPC reinforcement locations were selected as bottom reinforcement, two-side reinforcement, and U-shaped reinforcement, with all other conditions being equal. Figure 20 displays how the location of the UHPC reinforcement changes the load–deflection curves of secondary stressed T-beam specimens that are strengthened with UHPC. In Figure 20, we can see that the initial stiffness and peak load of the secondarily stressed T-beam specimens that were strengthened with UHPC gradually increase during the rising phase of the curve. This happened when the UHPC reinforcement location was moved from the bottom to the shape of a U.

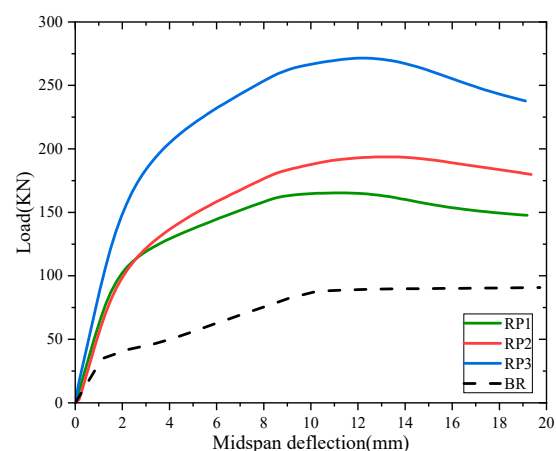


Figure 20. Results of UHPC reinforcement location analysis: load–deflection curves.

As shown in Table 8, compared with the original T-beam specimens, when the reinforcement location is the bottom reinforcement, the amplitude of load lifting is 76.4 KN, the multiplier of UHPC material used is 1 times, the load enhancement is 0.9 times, and

the material utilization rate is 0.9, while when the reinforcement location is changed to the reinforcement on both sides, the amplitude of load lifting is 104.8 KN, the multiplier of UHPC material used is 3.2 times of that of the bottom reinforcement, the load enhancement is 1.2 times, and the material utilization rate is 0.4. When the reinforcement location is changed to U-shaped reinforcement, the amplitude of load lifting is 182.5 KN, the UHPC material use multiplier is 4.6 times that of the bottom reinforcement, the load enhancement is 2.1 times, and the material utilization rate is 0.5.

Table 8. Comparison of reinforcement materials and peak loads.

	UHPC Material Usage/m ³	Material Use Multiplier	Peak Load/KN	Amplitude of Load Lifting/KN	Load Lifting Multiplier	Material Utilization Rate
bottom side	0.6	1	165.4	76.4	0.9	0.9
both sides	2	3.2	193.7	104.8	1.2	0.4
U-shape	2.9	4.6	271.5	182.5	2.1	0.5

Note: Amplitude of load lifting: peak load of strengthened T-beam–peak load of original T-beam; material utilization rate: load lifting multiplier/material use multiplier.

It can be seen that when the reinforcement location is located in a U-shaped reinforcement, the amplitude of load lifting is the greatest, but the material utilization rate is not high. The amplitude of load lifting of the two-side reinforcement is not significant compared to the bottom reinforcement, but it has the lowest material utilization rate. The bottom reinforcement has a more obvious load enhancement and the highest material utilization rate, which has the highest economic value in the actual project. As a result, it is recommended that the bottom reinforcement is the most appropriate location for economic and safety reasons.

5.3.4. Thickness of the Reinforcement Layer

In this section, the thickness of the reinforcement layer is selected to be 10 mm, 30 mm, 50 mm, 70 mm, and 90 mm, with all other conditions being equal. Figure 21 shows the effect of the thickness of the reinforcement layer on the load–deflection curves of the strengthened beams. Table 9 shows the characteristic loads of these beams. The results show that the flexural capacity and pre-yield stiffness of the longitudinal rebars increased as the thickness of the UHPC layer increased from 10 mm to 90 mm. This is due to the fact that the increase in the thickness of the UHPC increases the cross-sectional height of the reinforced beams and the internal force arm of the longitudinal rebars in the UHPC layer, thus effectively increasing the overall moment of inertia. In addition, UHPC applied to strengthened beams is characterized by high strain hardening under direct tensile loading. Increasing the thickness of UHPC improves the contribution of UHPC tensile strength to the cracking control and flexural load capacity of the reinforced beams. Moreover, it was found in Figure 21 that strengthened beams with thinner reinforcement layer thicknesses had better ductile behavior than those with thicker reinforcement layer thicknesses.

Table 9. Peak load comparison.

Parametric	Characteristic Load			
	Crack Load/KN	Rate of Increase	Peak Load/KN	Rate of Increase
BR	30	1	88.9	1
RT1	37.3	1.2	100.7	1.1
RT2	65.2	2.2	146.7	1.7
RT3	77.3	2.6	165.4	1.9
RT4	90.4	3.0	182.5	2.1
RT5	110.5	3.7	203.4	2.3

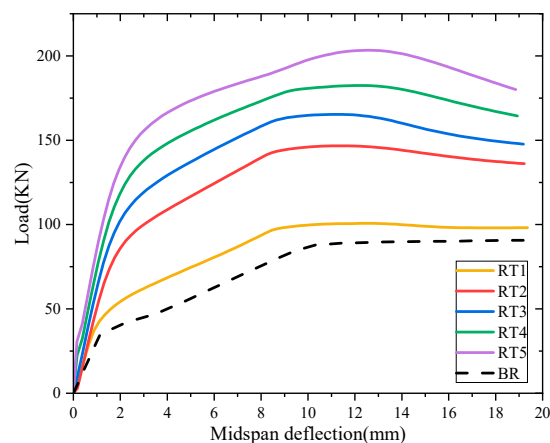


Figure 21. Results of the analysis of the thickness of the reinforcement layer: load–deflection curves.

6. Conclusions

This paper uses ABAQUS to investigate the flexural performance of damaged T-beams strengthened with UHPC using the post-installed rebar bonding technique. Using the post-installed rebar bonding technique, finite element simulations of push-out tests were first used to study the shear performance of the interface between UHPC and RC. The following primary conclusions were reached after the flexural performance of UHPC-strengthened damaged concrete T-beams was numerically simulated using the push-out test results from the finite element simulation:

- (1) The finite element simulation methods used in this paper are all very accurate. The load–deflection curves, load–midspan displacement curves, peak loads, and failure modes that were found from the simulations match the test results very well.
- (2) Through the push-out test finite element simulation, this paper proves that when the compressive strength of matrix concrete increases, the yield strength of shear-resistant steel bars continues to increase, and the anchorage capacity of shear-resistant steel bars is gradually enhanced. The horizontal spacing of shear-resistant steel bars is too small and easily causes local damage to the concrete substrate; the horizontal spacing of shear-resistant steel bars is too large and will cut the adhesive effect of the steel bar; the recommended horizontal spacing of shear-resistant steel bars of $8d\sim 12d$ is more reasonable. If the diameter of shear-resistant steel bars is too small or too large, it will reduce the interface shear strength and ductility of UHPC-RC. It is recommended that the diameter of shear-resistant steel bars be $10\sim 14$ mm.
- (3) Rebar shear friction and pinning force are the main sources of shear-bearing capacity at the UHPC-RC reinforcement interface. In this paper, the reinforcement shear friction force is taken into account as an influencing factor, and the shear capacity calculation formula of the old and new concrete interface in the Technical Specification for Assembled Concrete Structures is optimized. The proposed shear capacity calculation formula of the UHPC-RC reinforcement interface is more suitable for the actual situation.
- (4) It was discovered that the damaged T-beam can achieve a more satisfactory reinforcement effect when the layout form of the post-installed reinforcing bars is a square-shaped form and the longitudinal spacing of the post-installed reinforcing bars is 300 mm. The parametric analysis's findings demonstrated that as the longitudinal spacing of the post-installed reinforcing bars increased beyond 300 mm, the strengthened beams' flexural performance dramatically declined. The cracking load and peak load of the strengthened beams were greatly increased by the increase in the thickness of the reinforcement layer. From the point of view of safety and economy, the UHPC-strengthened position is recommended to be the bottom reinforcement. However, the reinforcement effect of the three different reinforcement locations with the same amount of UHPC material is a question worth studying.

It should be pointed out that, although several key parameters concerning the shear strength of the UHPC-RC interface have been investigated in this paper, in order to more comprehensively explore the influencing factors affecting UHPC-strengthened T-beams, control variable studies should be carried out on these key parameters at a later stage in view of the differences in the steel bar adhesive, steel bar placement, and casting direction adopted in the actual reinforcement project. And it is not clear why the results of strengthening T-shaped beams are different from those of strengthening rectangular beams, and control variable studies should also be carried out on the basis of this problem at a later stage. Based on the U-shaped reinforcement structure using UHPC, a control variable study on the relationship between bottom thickness and side thickness can be carried out to specify a more reasonable configuration of the U-shaped reinforcement structure.

Author Contributions: Conceptualization, Y.L. and J.Y.; methodology, Y.L. and J.Y.; software, Y.L.; validation, Y.L.; data curation, Y.L.; writing—original draft preparation, Y.L.; writing—review and editing, J.Y., J.D., Z.J. and K.Z.; supervision, J.Y.; project administration, J.Y. and J.D.; funding acquisition, J.Y. All authors have read and agreed to the published version of the manuscript.

Funding: This research was funded by the National Natural Science Foundation of China, grant number 52278293; and the 2023 Chongqing University Student Innovation and Entrepreneurship Training Program National Project “Research on the Bending and Bearing Capacity of UHPC Strengthened T-Beams”, grant number 202310618014.

Institutional Review Board Statement: Not applicable.

Informed Consent Statement: Not applicable.

Data Availability Statement: The data presented in this study are available upon reasonable request from the corresponding author.

Conflicts of Interest: The authors declare no conflicts of interest.

References

1. Zhou, X.; Zhang, X. Thoughts on the development of bridge technology in China. *Engineering* **2019**, *5*, 1120–1130. [[CrossRef](#)]
2. Pape, T.M.; Melchers, R.E. The effects of corrosion on 45-year-old pre-stressed concrete bridge beams. *Struct. Infrastruct. Eng.* **2011**, *7*, 101–108. [[CrossRef](#)]
3. Luo, Y.; Zheng, H.; Zhang, H.; Liu, Y. Fatigue reliability evaluation of aging prestressed concrete bridge accounting for stochastic traffic loading and resistance degradation. *Adv. Struct. Eng.* **2021**, *24*, 3021–3029. [[CrossRef](#)]
4. Prasanna, P.; Dana, K.J.; Gucunski, N.; Basily, B.B.; La, H.M.; Lim, R.S.; Parvardeh, H. Automated crack detection on concrete bridges. *IEEE Trans. Autom. Sci. Eng.* **2014**, *13*, 591–599. [[CrossRef](#)]
5. Zhan, Y.; Dong, S.; Zhao, Y.; Zhao, Z.; Chen, X.; Du, H.; Wang, F. *CICTP 2023: Analysis of Deformation Law of Construction Supports of Bridge Engineering under Insufficient Foundation Bearing Capacity*; ASCE Press: Boca Raton, FL, USA, 2023; pp. 471–481.
6. Bonopera, M.; Chang, K.-C. Novel method for identifying residual prestress force in simply supported concrete girder-bridges. *Adv. Struct. Eng.* **2021**, *24*, 3238–3251. [[CrossRef](#)]
7. Wang, W.; Gong, J.; Wu, X.; Wang, X. A general equation for estimation of time-dependent prestress losses in prestressed concrete members. In *Structures*; Elsevier: Amsterdam, The Netherlands, 2023; pp. 278–293.
8. Wardhana, K.; Hadipriono, F.C. Analysis of recent bridge failures in the United States. *J. Perform. Constr. Facil.* **2003**, *17*, 144–150. [[CrossRef](#)]
9. Richard, P.; Cheyrezy, M.H. Reactive powder concretes with high ductility and 200–800 MPa compressive strength. *Spec. Publ.* **1994**, *144*, 507–518.
10. De Larrard, F.; Sedran, T. Optimization of ultra-high-performance concrete by the use of a packing model. *Cem. Concr. Res.* **1994**, *24*, 997–1009. [[CrossRef](#)]
11. Zhang, Y.; Zhu, Y.; Yeseta, M.; Meng, D.; Shao, X.; Dang, Q.; Chen, G. Flexural behaviors and capacity prediction on damaged reinforcement concrete (RC) bridge deck strengthened by ultra-high performance concrete (UHPC) layer. *Constr. Build. Mater.* **2019**, *215*, 347–359. [[CrossRef](#)]
12. Wang, J.; Liu, J.; Wang, Z.; Liu, T.; Liu, J.; Zhang, J. Cost-effective UHPC for accelerated bridge construction: Material properties, structural elements, and structural applications. *J. Bridge Eng.* **2021**, *26*, 04020117. [[CrossRef](#)]
13. Zhou, M.; Lu, W.; Song, J.; Lee, G.C. Application of ultra-high performance concrete in bridge engineering. *Constr. Build. Mater.* **2018**, *186*, 1256–1267. [[CrossRef](#)]
14. Xue, J.; Briseghella, B.; Huang, F.; Nuti, C.; Tabatabai, H.; Chen, B. Review of ultra-high performance concrete and its application in bridge engineering. *Constr. Build. Mater.* **2020**, *260*, 119844. [[CrossRef](#)]

15. Fehling, E.; Schmidt, M.; Walraven, J.; Leutbecher, T.; Fröhlich, S. *Ultra-High Performance Concrete UHPC*; Ernst & Sohn: Berlin, Germany, 2014; pp. 25–32.
16. Wang, Y.Z.; Wang, Y.B.; Zhao, Y.Z.; Li, G.Q.; Lyu, Y.F.; Li, H. Experimental study on ultra-high performance concrete under triaxial compression. *Constr. Build. Mater.* **2020**, *263*, 120225. [[CrossRef](#)]
17. Kang, S.T.; Lee, Y.; Park, Y.D.; Kim, J.K. Tensile fracture properties of an Ultra High Performance Fiber Reinforced Concrete (UHPC) with steel fiber. *Compos. Struct.* **2010**, *92*, 61–71. [[CrossRef](#)]
18. Wille, K.; El-Tawil, S.; Naaman, A.E. Properties of strain hardening ultra high performance fiber reinforced concrete (UHP-FRC) under direct tensile loading. *Cem. Concr. Compos.* **2014**, *48*, 53–66. [[CrossRef](#)]
19. Wu, P.; Wu, C.; Liu, Z.; Hao, H. Investigation of shear performance of UHPC by direct shear tests. *Eng. Struct.* **2019**, *183*, 780–790. [[CrossRef](#)]
20. Lampropoulos, A.P.; Paschalis, S.A.; Tsioulou, O.T.; Dritsos, S.E. Strengthening of reinforced concrete beams using ultra high performance fibre reinforced concrete (UHPC). *Eng. Struct.* **2016**, *106*, 370–384. [[CrossRef](#)]
21. Zhu, Y.; Zhang, Y.; Hussein, H.H.; Chen, G. Flexural strengthening of reinforced concrete beams or slabs using ultra-high performance concrete (UHPC): A state of the art review. *Eng. Struct.* **2020**, *205*, 110035. [[CrossRef](#)]
22. Fang, Z.; Fang, S.; Liu, F. Experimental and numerical study on the shear performance of short stud shear connectors in steel-UHPC composite beams. *Buildings* **2022**, *12*, 418. [[CrossRef](#)]
23. Hung, C.C.; El-Tawil, S.; Chao, S.H. A review of developments and challenges for UHPC in structural engineering: Behavior, analysis, and design. *J. Struct. Eng.* **2021**, *147*, 03121001. [[CrossRef](#)]
24. TTanarlan, H.M.; Alver, N.İ.; Jahangiri, R.; Yağcıncaya, Ç.; Yazıcı, H. Flexural strengthening of RC beams using UHPC laminates: Bonding techniques and rebar addition. *Constr. Build. Mater.* **2017**, *155*, 45–55. [[CrossRef](#)]
25. Tanarlan, H.M. Flexural strengthening of RC beams with prefabricated ultra high performance fibre reinforced concrete laminates. *Eng. Struct.* **2017**, *151*, 337–348. [[CrossRef](#)]
26. Safdar, M.; Matsumoto, T.; Kakuma, K. Flexural behavior of reinforced concrete beams repaired with ultra-high performance fiber reinforced concrete (UHPC). *Compos. Struct.* **2016**, *157*, 448–460. [[CrossRef](#)]
27. Hong, S.G.; Kang, S.H. Effect of surface preparation and curing method on bond strength between UHPC and normal strength concrete. In Proceedings of the IABSE Conference: Structural Engineering: Providing Solutions to Global Challenges, Geneva, Switzerland, 23–25 September 2015; pp. 1537–1543.
28. Jang, H.O.; Lee, H.S.; Cho, K.; Kim, J. Experimental study on shear performance of plain construction joints integrated with ultra-high performance concrete (UHPC). *Constr. Build. Mater.* **2017**, *152*, 16–23. [[CrossRef](#)]
29. Banjara, N.K.; Ramanjaneyulu, K. Experimental and numerical study on behaviour of HSFRC overlay strip strengthened flexural deficient RC beams. *Eng. Struct.* **2019**, *198*, 109561. [[CrossRef](#)]
30. Al-Osta, M.A.; Isa, M.N.; Baluch, M.H.; Rahman, M.K. Flexural behavior of reinforced concrete beams strengthened with ultra-high performance fiber reinforced concrete. *Constr. Build. Mater.* **2017**, *134*, 279–296. [[CrossRef](#)]
31. Pimentel, M.; Nunes, S. Experimental tests on RC beams reinforced with a UHPC layer failing in bending and shear. In Proceedings of the 4th International Symposium on Ultra-High Performance Concrete and High Performance Materials, Kassel, Germany, 9–11 March 2016; pp. 9–11.
32. Liu, T.; Charron, J.-P. Characterization of interface properties for modeling the shear behavior of T-beams strengthened with ultra high-performance concrete. In *Structure and Infrastructure Engineering*; Taylor & Francis: Abingdon, UK, 2023; pp. 1–16.
33. Liu, T.; Charron, J.-P. Experimental study on the shear behavior of UHPC-strengthened concrete T-beams. *J. Bridge Eng.* **2023**, *28*, 04023064. [[CrossRef](#)]
34. Sun, W.; Fan, W.; Yang, J.; Zhang, Y.; Zhong, Z. Interfacial shear performance of UHPC-strengthened RC structures using post-installed rebar connections: Experiments and analyses. *Eng. Struct.* **2023**, *277*, 115411. [[CrossRef](#)]
35. Gao, X.L.; Wu, K.; Guo, Y.Q.; Zhao, Y.C.; Guo, J.Y. Experimental and numerical study on flexural behaviors of damaged RC beams strengthened with UHPC layer using the bonding technology of post-installed reinforcing bar. *Constr. Build. Mater.* **2023**, *391*, 131835. [[CrossRef](#)]
36. Zhu, Y.; Zhang, Y.; Li, X.; Chen, G. Finite element model to predict structural response of predamaged RC beams reinforced by toughness-improved UHPC under unloading status. *Eng. Struct.* **2021**, *235*, 112019. [[CrossRef](#)]
37. Cladera, A.; Marí, A.; Ribas, C.; Bairán, J.; Oller, E. Predicting the shear–flexural strength of slender reinforced concrete T and I shaped beams. *Eng. Struct.* **2015**, *101*, 386–398. [[CrossRef](#)]
38. Börgesson, L. Abaqus. In *Developments in Geotechnical Engineering*; Elsevier: Amsterdam, The Netherlands, 1996; Volume 79, pp. 565–570.
39. General Administration of Quality Supervision, Inspection and Quarantine of the People’s Republic of China; National Standardization Administration of China. *GB/T 1499.2-2018*; Steel for the Reinforcement of Concrete—Part 2: Hot Rolled Ribbed Bars. Chinese Specification Press: Beijing, China, 2018. (In Chinese)
40. Zhang, J.; Xu, Y.; Mai, Z.; Lv, W. Flexural performance of RC T-beams strengthened with external double steel channel. *J. Build. Eng.* **2021**, *42*, 102453. [[CrossRef](#)]
41. Ministry of Housing and Urban-Rural Development of the People’s Republic of China. *GB 50010-2010*; Code for Design of Concrete Structures. Standardization Administration of China: Beijing, China, 2010. (In Chinese)

42. Zhang, Z.; Shao, X.D.; Li, W.G.; Zhu, X.; Chen, H. Axial tensile behavior test of ultra high performance concrete. *China J. Highw. Transp.* **2015**, *28*, 50.
43. Yang, J.; Fang, Z. Research on stress-strain relation of ultra high performance concrete. *Concrete* **2008**, *7*, 11–15.
44. Hussein, H.H.; Walsh, K.K.; Sargand, S.M.; Al Rikabi, F.T.; Steinberg, E.P. Modeling the shear connection in adjacent box-beam bridges with ultrahigh-performance concrete joints. I: Model calibration and validation. *J. Bridge Eng.* **2017**, *22*, 04017043. [[CrossRef](#)]
45. ACI Committee. *Building Code Requirements for Structural Concrete and Commentary*; ACI 318; American Concrete Institute: Farmington Hills, MI, USA, 2014; Volume 14.
46. American Association of State Highway and Transportation Officials. *AASHTO LRFD Bridge Design Specifications*; American Association of State Highway and Transportation Officials: Washington, DC, USA, 2020.
47. The International Federation for Structural Concrete. *Fib Model Code for Concrete Structures 2010*; The International Federation for Structural Concrete: Lausanne, Switzerland, 2013.
48. Ministry of Transport of the People's Republic of China. *JTG/T J22-2008*; Code for Design of Highway Bridge Reinforcement. China Communications Press: Beijing, China, 2015. (In Chinese)
49. Ministry of Housing and Urban-Rural Development of the People's Republic of China. *JGJ1-2014*; Technical Specification for Prefabricated Concrete Structures. China Building Industry Press: Beijing, China, 2014. (In Chinese)

Disclaimer/Publisher's Note: The statements, opinions and data contained in all publications are solely those of the individual author(s) and contributor(s) and not of MDPI and/or the editor(s). MDPI and/or the editor(s) disclaim responsibility for any injury to people or property resulting from any ideas, methods, instructions or products referred to in the content.